

Numerical Studies of Depressurization-Induced Gas Production from an Interbedded Marine Turbidite Gas Hydrate Reservoir Model

Evgeniy M. Myshakin,^{1,2*} Jeen-Shang Lin,^{1,3} Shun Uchida,^{1,4} Yongkoo Seol,¹
Timothy S. Collett,⁵ Ray Boswell¹

¹ U.S. Department of Energy, National Energy Technology Laboratory, 626 Cochran's Mill Road, Pittsburgh, Pennsylvania, USA

² AECOM, 626 Cochran's Mill Road, Pittsburgh, Pennsylvania, USA

³ Department of Civil and Environmental Engineering, University of Pittsburgh, Pittsburgh, Pennsylvania, USA

⁴ Department of Civil and Environmental Engineering, Rensselaer Polytechnic Institute, Troy, New York, Pennsylvania, USA

⁵ U.S. Geological Survey, Denver, Colorado, USA

* Corresponding author: evgeniy.myshakin@netl.doe.gov

Abstract

The numerical simulation of thin hydrate-bearing sand layers interbedded with mud layers is investigated. In this model, the lowest hydrate layer occurs at the base of gas hydrate stability and overlies a thinly-interbedded saline aquifer. The predicted gas rates reach 6.25 MMscf/day ($\sim 1.77 \times 10^5 \text{ m}^3/\text{day}$) after 90 days of continuous depressurization with manageable water production. Development of horizontal dissociating interfaces between hydrate-bearing sand and mud layers is a primary determinant of reservoir performance. A set of simulations has been executed to assess uncertainty in *in situ* permeability and to determine the impact of the saline aquifer on productivity.

Introduction

Methane hydrates represent crystalline ice-like compounds where the gas molecules are encapsulated within water cages of the hydrate lattice. Moderate pressure and relatively low temperature (273-290 K) are required to form methane hydrate.[1] The conditions favoring hydrate formation exist in sub-oceanic sediments, primarily continental shelf and slope regions, and in permafrost areas.[2] A cubic unit cell consists of 46 water molecules per 8 gas molecules.[1] As a result, the concentration of methane entrapped in hydrates is such that it exceeds the concentration in an equivalent reservoir volume of free gas at depth up to 1200-2000 m (4000-6000 ft, 12-20 MPa, depending on local conditions) below sea-level.[3] Because of abundance in nature and high "energy density" per unit volume methane hydrates are considered a potentially vast energy source.[4]

Gas hydrate deposits can occur as seafloor mounds, within fractures, in the form of veins and nodules, and as pore-fill in silt and sand accumulations. At present, given known technologies, the gas hydrate technical recoverability using conventional well drilling approaches is limited to sand reservoirs.[3] As host media, sand sediments in both arctic and marine environment provide high intrinsic permeability (up to 1 Darcy) and high pore space that can be filled with gas hydrate in the range of 60-90%.[5] In the marine environment, gas hydrate depositions were confirmed in multiple drilling programs conducted around the world, including the discovery of gas hydrate-bearing sands on the Cascadia margin,[6] in the Nankai Trough,[7] in the Gulf of Mexico,[8], in the Krishna-Godavari Basin of offshore India,[9]. Gas hydrate occurrence were found in silty clay sediments of South China Sea,[10] as sequences of fracture-fills in offshore Malaysia,[11] Korea,[12] India,[13] and in the Gulf of Mexico.[8] The first field trial of gas production from a marine gas hydrate deposit was conducted in the Eastern Nankai Trough off the Pacific Ocean near Japan in 2013.[14]

In support of planning, execution, and analyzing results of field production tests, numerical simulations serve as a low-cost way to estimate gas hydrate reservoir response to hydrate destabilization using various gas production

scenarios, methods, and well designs. Recent numerical simulation studies of gas hydrate accumulations explore production potential by means of depressurization of marine hydrate-bearing sediments in the Gulf of Mexico,[15,16] Ulleung Basin in the Korean East Sea,[17] the Shenhu area in the South China Sea,[18] and the Eastern Nankai Trough, Japan.[19,20] This study is focused evaluation of hypothetical thin-bedded gas reservoirs in ultra-deepwater. Such accumulations are likely to occur in many deepwater systems and proper geological interpretation of well logs could be obscured due to limited resolution of logging tools.[21] The initial gas production is heavily depended on *in situ* permeability of hydrate-bearing porous media and accounting for variability of that parameter is vital to reliably predict production potential [14,22]. The simulations were carried out to evaluate reservoir productivity using two values of *in situ* permeability based on recent borehole pressure-transient testing and pressurized core measurements.

Geologic input model

The reservoir model was created based on an existing hydrate-bearing marine accumulation that is characterized with a set of well logs. Water depth at that location is 2,575 m and hydrate stability zone extends to approximately 300 m. The reservoir is located at similar depths as for the Gulf of Mexico hydrate-bearing (“blue” and “orange”) sands, 2,000 m of water depth and 800 mbsf (meters below sea floor) of burial depth,[16] but deeper than the hydrate accumulation at the eastern Nankai Trough production test site. That deposit exists at approximately 1,000 m of water depth and 300 mbsf within sandy turbidite sediments.[14]

The two-dimensional (2D) model consists of five major lithologic units, each containing a large number of individual sub-units (Figure 1 and Table 1). Unit 1 encompasses high-porosity mud-rich sediments from the sea-floor to a depth 151 mbsf. Unit 2 represents a zone of low-saturation accumulation of gas hydrate as massive fracture-filling veins and lenses within a mud-rich sediment from 151–244 mbsf. Unit 2 includes 93 modeled sub-units each 1 m in thickness. Unit 3 is a section of uniform marine muds with no gas hydrate occurrence extending from 244–278.8 mbsf. Unit 4 represents the interbedded sand and mud sub-units from 272.8 to 296.9 mbsf. From 272.8 to 290.6 mbsf, eighteen sand sub-units (#1-18) are highly-saturated with gas hydrate. From 290.6 to 296.9 mbsf, sand sub-units within the lower part of Unit 4 are water-bearing only. The deepest hydrate-bearing sand sub-unit 18th is at the base of gas hydrate stability (BGHS) in contact with the water-bearing sand sub-unit (Figure 1). All interbedded muds within Unit 4 are interpreted as water-bearing with no gas hydrate. To provide greater fidelity to the thin-bedded nature of the primary reservoir unit, Unit 4 is modeling using 241 separate sub-units of variable lithology, each 0.1 m thick (Table 1). Unit 5 extends from 296.6 to 496.9 and is a section of uniform marine muds with no gas hydrate present. The thickness of Unit 5 is somewhat arbitrary, but was assigned a thickness of 200 m to provide adequate separation between the primary reservoir interval in Unit 4 and the base of the geologic model.

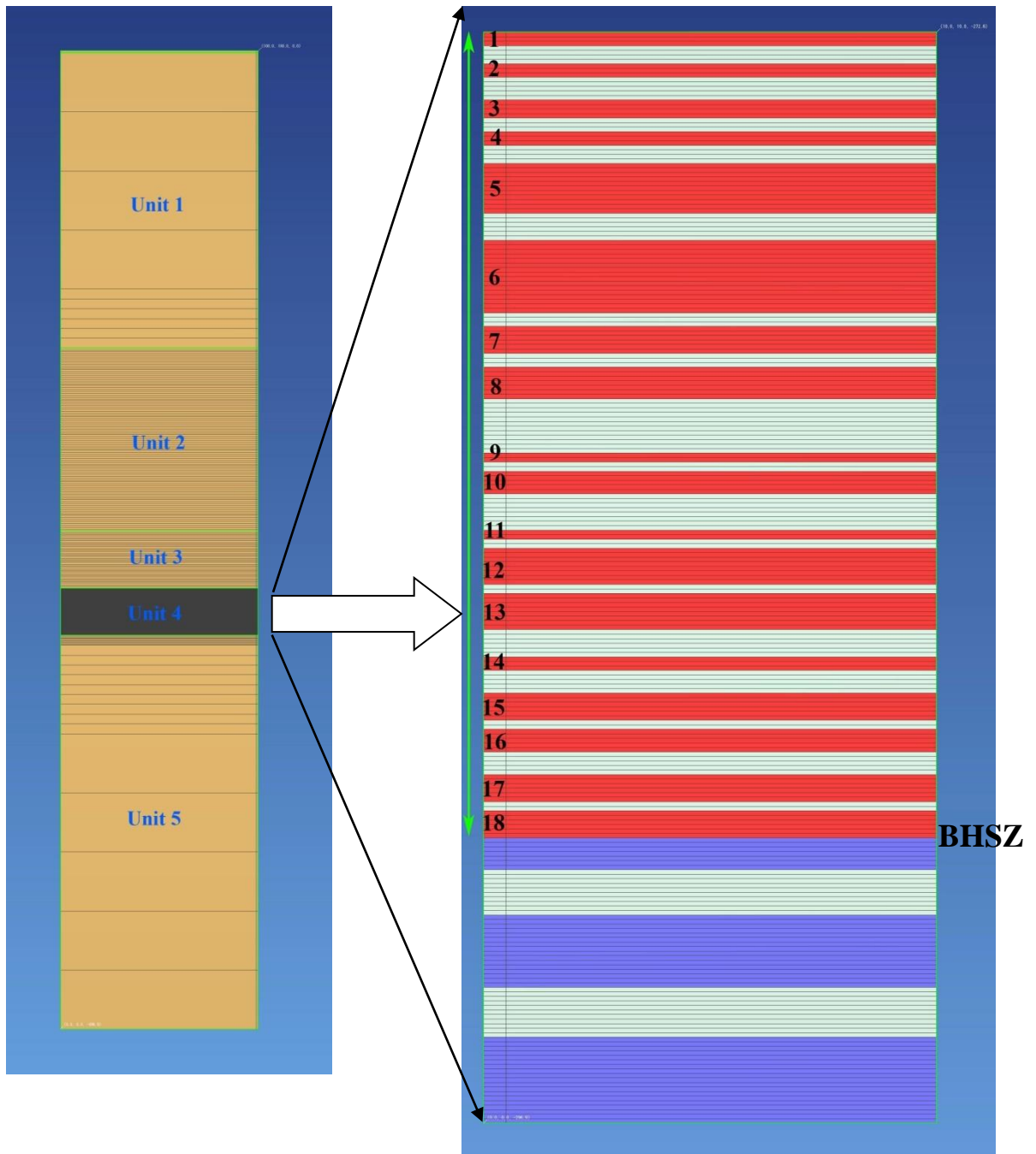


Figure 1: 2D model incorporating all lithologic units (left), and expanded view of Unit 4 (right), where RED designates hydrate-bearing sand reservoir layers (sub-units #1-18); BLUE are water-bearing sand reservoir layers; GRAY are non-reservoir mud layers. BHSZ means boundary of hydrate stability zone at 290.6 mbsf. The green arrow indicates the interval completion for a vertical well bore.

Table 1: The reservoir model geometry.

Major Model Unit	Log Measured Depth ¹	Sub-seafloor Depth ²	Thickness (m)	Subunits
UNIT 1: uniform marine mud with no hydrate	2,575.0–2,726.0	0.0–151.0	151.0	1 @ 31 m 3 @ 30 m 6 @ 5 m
UNIT 2: uniform marine mud with fracture filled gas hydrate	2,726.0–2,819.0	151.0–244.0	93.0	93 @ 1 m
UNIT 3: uniform marine mud with no hydrate	2,819.0–2,847.8	244.0–272.8	28.8	36 @ 0.8 m
UNIT 4: Interbedded hydrate-bearing sand and hydrate-free mud	2,847.8–2,871.9	272.8–296.9	24.1	241 @ 0.1 m
UNIT 5: uniform marine mud with no hydrate	2,871.9–3,071.9	296.9–496.9	200.0	10 @ 0.5 m 9 @ 5 m 5 @ 30 m
Total	2,575.0–3,071.9	0.0–496.9	496.9	404 @ var.

¹ Meters below rotary table (rig rotary table above sea level: 28.5 m)

² Meters below sea floor

The vertical discretization of the geologic model based on well data was extended laterally from the wellbore. A lateral distance of 500 m is used to extend the units observed at the well location. No flow and no heat exchange through lateral sides of the cylindrical reservoir domain were allowed. The top of Unit 1 (the seafloor) and the bottom of Unit 5 are set at fixed boundary conditions to maintain constant temperature according to the geothermal gradient. Taking advantage of the cylindrical symmetry, the 2D model was created using one hundred grid blocks with logarithmically distributed lengths from $r_w = 0.15$ m to $r_{100} = 500$ m horizontally providing fine discretization around the wellbore. The total number of grid blocks representing the reservoir domain is 35,905 with 71,354 connections. Simulation tests were conducted with an increased number of grid blocks in the lateral direction to confirm that numerical results are independent of the selected mesh resolution.

Initial conditions

The pressure in the sediment subsurface was assumed to follow a hydrostatic pore pressure distribution, the assumption supported by measurements taken in natural hydrate deposits.[23] To determine thermal distribution throughout the reservoir model the local geothermal gradient equal to $^{\circ}\text{C} = 0.0663 \times \text{mbsf} + 1.9855$ $^{\circ}\text{C}$ (surface temperature). Pore water salinity was taken to be 35 ppt, a typical number for seawater. The temperature depression induced by salt presence in the aqueous phase on the equilibrium pressure-temperature (P/T) relationship was computed internally in the code through the equation of Dickens and Quinby-Hunt.[24] Following a hydrostatic pressure distribution, the estimated geothermal gradient and accounting for the salinity, the pressure and temperature conditions at BHSZ (Figure 1) was computed to be $P_{eq} = 28.73$ MPa and $T_{eq} = 19.89$ $^{\circ}\text{C}$. For the layers of the reservoir model proper initialization of initial P/T conditions (pressure and temperature gradients throughout the vertical dimension of the domain) is needed to achieve hydraulic, thermal, thermodynamic, and chemical equilibrium and ensure correct location of the layers relative to BHSZ. To do that a procedure similar to that reported in [25] was used. Initial pressure and temperature distributions within the 2D model are shown in Figure 2. The location of BHSZ below the deepest hydrate-bearing sand layer means that even slightest pressure reduction would promptly induce hydrate decomposition. The temperature profile shows that the gas hydrate exists within the 19-20 $^{\circ}\text{C}$ interval providing ample sensible heat to maintain the hydrate decomposition reaction. Thus, the pressure and temperature conditions favor the depressurization method as a tool to destabilize hydrate for gas production.

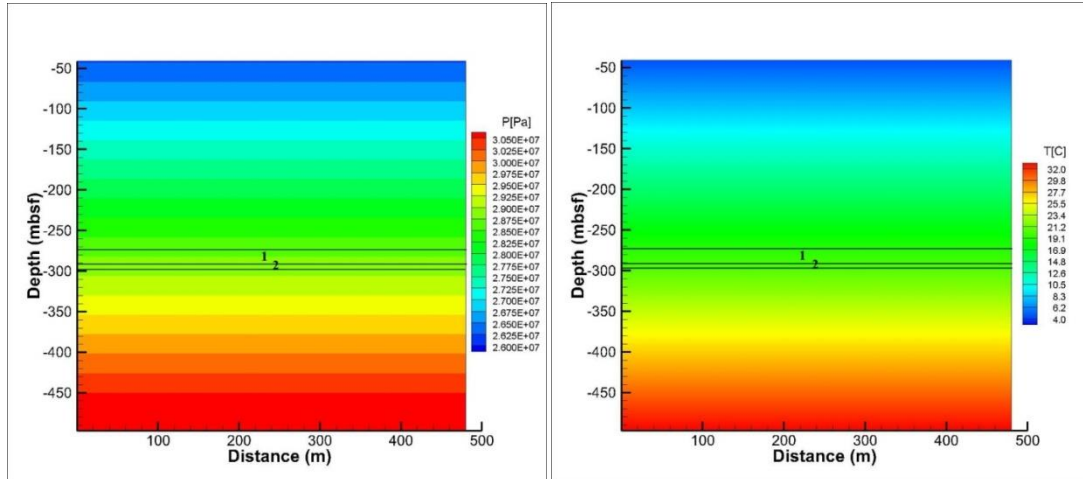


Figure 2: Initial pressure (left) and temperature (right) distributions within the model. **1** stands for the interbedded hydrate-bearing sand section; **2** designates water-bearing sand section of the reservoir.

Modeled production well

To conduct the simulations, a vertical well was constructed at the center of the cylindrical domain. The well is completed (no sand control is included in the well set-up at this time as these initial runs do not include potential grain movement or other geomechanical considerations) throughout the hydrate-bearing sand sub-units and the mud-rich interbedded sub-units in Unit 4 (from 272.8 to 290.6 mbsf; the green arrow in Figure 1). The hole is open to production from the top of Unit 4, (the top of hydrate bearing sub-unit #1) to the contact between the deepest hydrate-bearing sand (sub-unit #18) and the underlying water-bearing sand sub-unit (Figure 1). To explore sensitivity of production to the presence of the thinly-bedded aquifer beneath sub-unit #18, another well completion was applied from 272.8 (sub-unit #1) to 289.8 mbsf (sub-unit #17). That essentially separates the producing hydrate-bearing units from the water-bearing sand by means of the interval including the mud sub-unit and sub-unit #18 (Figure 1). Depressurization is simulated by applying a constant pressure of 3.0 MPa at the topmost grid block of the wellbore sub-domain located just above the top of Unit 4 (sub-unit #1, Figure 1). The wellbore sub-domain was represented using the pseudoporous-medium approach.[26]

Simulation cases

This 2D reservoir model uses an idealized, homogeneous description of saturation and porosity of hydrate-bearing sand and mud sub-units. The intrinsic permeability of sand was assumed to be 1 Darcy and mud sections were assigned with low permeability value, 5×10^{-4} md. The other parameters given in Table 2 were taken from the literature data including the use of Nankai Trough data as an analogue.[27,29] Effective (aqueous) permeability reflects reduced ability of porous media to transmit fluid due to presence of solid (hydrate) phase and/or emerging gas phase. The effective permeability is calculated using a relative permeability function and a porosity-permeability relationship to modify intrinsic permeability. Previous works, based primarily on short-duration borehole pressure-transient testing in Alaska, had generally indicated a low value of the effective permeability, such as 0.1 md.[28] However, recent evaluations of pressure cores acquired in Japan suggest *in situ* permeability of hydrate-bearing sands may range from 1 to 100 md measured for pressurized core sediments.[29] To encompass uncertainty in effective permeability evaluations, two cases were created, Case 1A uses 0.1 md that approximately captures a lower boundary of the value and Case 1B features a 10 md value for the upper boundary. Those values of initial effective permeability were achieved by adjusting the corresponding the power n_A value for the relative permeability function (Table 3) with assumptions of 80% for initial hydrate saturation and 10% for bound water (Table 2). The Original Porous Media (OPM) model was used implying that porosity is divided

Table 2: Initial hydrate reservoir parameters.

Formation Unit	Porosity (frac)	Hydrate Saturation (%)	Free water Saturation (%)	Bound water Saturation (%)	Intrinsic Permeability, (md) *	Effective Permeability, (md)*	Thermal conductivity of porous media, dry/wet(W/m K)****	Pore compressibility (Pa ⁻¹)	Rock density (kg/m ³)	Rock grain specific heat (J/kg °C)
1	67	0	10	90	5x10 ⁻⁴	5x10 ⁻⁴	0.17 / 1.16	1.2x10 ⁻⁸	2750	1000
2	66	10	10	80	5x10 ⁻⁴	5x10 ⁻⁴	0.17 / 1.18	1.2x10 ⁻⁸	2600	1000
3	71	0	10	90	5x10 ⁻⁴	5x10 ⁻⁴	0.15 / 1.07	1.2x10 ⁻⁸	2700	1000
4 (GH sand)	40	80	10	10	10 ³	0.1 or 10**	0.37 / 2.28	1.2x10 ⁻⁸	2750	1000
4 (mud)	40	0	10	90	5x10 ⁻⁴	5x10 ⁻⁴	0.36 / 1.95	1.2x10 ⁻⁸	2750	1000
4 (H ₂ O sand)	40	0	90	10	10 ³	10 ³	0.37 / 2.28	1.2x10 ⁻⁸	2750	1000
5	53	0	10	90	5x10 ⁻⁴	5x10 ⁻⁴	0.24 / 1.51	1.2x10 ⁻⁸	2650	1000

*Values are for the horizontal permeabilities; a 0.1 coefficient is used for horizontal permeabilities; ** Cases 1A and 2A accept 0.1 md and Cases 1B and 2B assume 10 md; ***Maxwell mixing rule[31] was applied to estimated dry and wet (water saturated) thermal conductivities using 5.1 W/m K for rock; 0.6 W/mK for water and hydrate, and 0.07 W/mK for methane.

between hydrate, water, and gas and effective permeability is controlled by the relative saturations of those phases in pores.[30] Table 3 also collects the parameters of the capillary pressure function used in the simulations.

Cases 1A and 1B were carried out to predict reservoir performance using the perforated interval to induce depressurization in all hydrate-bearing sub-units including the deepest #18 that is in contact with the aquifer (Figure 1). Cases 2A and 2B, assuming 0.1 and 10 md of effective permeability, respectively, were conducted with the shortened perforated interval as explained in the “Modeled production well” section above.

Simulations of gas production from the 2D models were performed using a parallel version of TOUGH+Hydrate code[30] developed to model the non-isothermal gas release, phase behavior, and flow of fluids and heat in complex geological media.

Table 3: Capillary pressure and relative permeability models.

Capillary pressure model[32]	$\bar{s}_l = \frac{(s_l - s_{lr})}{(1 - s_{lr})} = \left[1 - \left(\alpha \beta_{gl} \left\{ \frac{(P_g - P_l)}{\rho_l g} \right\} \right)^n \right]^{-m}$ $\alpha = 10.204 \text{ 1/m}, \beta_{gl} = 1.0, n = 4.432, m = 0.7744, s_{lr} = 0.09 \quad [34]$
Relative permeability model[33]	$k_{rA} = (S_A^*)^{n_A} ; k_{rG} = (S_G^*)^{n_G}$ $S_A^* = \frac{(S_A - S_{irA})}{(1 - S_{irA})} ; S_G^* = \frac{(S_G - S_{irG})}{(1 - S_{irG})}$ $n_A = 4.20 \text{ (Cases 1A and 2A)} / 2.10 \text{ (Cases 1B and 2B)}; n_G = 3.16 \quad [34]$ <p>$S_A, S_G, S_{irA},$ and S_{irG} are aqueous, gas, irreducible aqueous, and irreducible gas saturations, respectively</p>

Simulation Results

Gas and water production

Figures 3-5 and 14-16 are organized in such way that each figure number designates two (left and right) figures. A left figure provides a time-dependent quantity during first 90 days of production, while a right one shows the same quantity change over 5 years of depressurization. Figures 3 and 14 compare the predicted gas rates and volumes for Cases 1A / 1B and Cases 1B / 2B, respectively (in Cases 2A the rates are extremely low and results are not included here). For the same pair of cases Figures 4 and 15 collect water rates and volumes and Figures 5 and 16 show the volumetric water-to-gas ratio dependency as a function of time. Table 4 provides values for gas and water rates/volumes at 30, 60, and 90 days.

The reservoir was predicted to produce gas at a rate from $7.86 \times 10^3 \text{ m}^3/\text{day}$ (0.28 MMscf/day) to $1.77 \times 10^5 \text{ m}^3/\text{day}$ (6.25 MMscf/day) after 90 days of depressurization for Case 1A and Case 1B, respectively. In Case 1B the production gas rate is comparable with the $8.0 \times 10^4 \text{ m}^3/\text{day}$ value predicted using depressurization of thinly-bedded oceanic hydrate accumulation at the eastern Nankai Trough (hydrate saturations up to 80% and initial effective permeability from 1 to 10 md were used for fine sand layers in that study).[14] Because of more intensive hydrate decomposition accompanying water release in the reservoir, production of water is higher at Case 1B comparing to Case 1A. After 90 days of depressurization, it is about 1.2×10^5 and $7.0 \times 10^4 \text{ m}^3$ of water produced at Case 1B and Case 1A, respectively. Those numbers are increased up to 5.8×10^5 and $2.5 \times 10^5 \text{ m}^3$ after 5 years of production. In spite of higher water production, the volumetric ratio measuring volume of water produced per 1 m^3 of gas (at standard P/T conditions) is consistently smaller for Case 1B than it is for Case 1A during the first 1.5 years. After that time, the ratio numbers converge to approximately 0.01 for two cases and stay relatively constant throughout the rest of the simulation period, 5 years. Given that the volumetric ratio of water-to-gas volumes released after decomposition of 1 m^3 of methane hydrate (at the hydration number equal to 6.0 and standard P/T conditions) is around 0.005, the stabilization of the ratio of produced water-to-gas volumes suggests that heat transfer supporting the decomposition reaction becomes a dominant factor controlling the production rates. For Case 1B the ratio becomes 0.1 after about 90 days of production, for Case 1A featuring the low effective permeability (that determines the ability of the reservoir to transmit fluids for effective depressurization) it takes more than a year to reach that value.

Water management during gas production from hydrates is an important aspect of commercially viable reservoir exploitation. The necessity to lift a significant amount of brine to the sea level poses a number of technological challenges contributing into an overall project cost. The interbedded nature of this hydrate reservoir provides an opportunity to “disconnect” the producing sub-units from the aquifer, which is in contact with hydrate-bearing sub-unit #18, by means of the new well completion design. The design implies modification of the completed interval to the bottom of the sub-unit #17 separated from #18 and the aquifer by a low permeability mud sub-unit. The results of Case 2A show that gas production rate declines by more than an order of magnitude during first 90 days (with similar trend predicted for longer times) and the produced gas volume is two orders of magnitude smaller than that predicted at Case 1A. That means that reservoir performance is determined by the productivity from the deepest hydrate-bearing sub-unit #18 benefiting from the enhanced depressurization along the hydrate-water contact (under conditions of impermeable for mass flow lateral boundaries). In contrast to Case 2A, the productivity using Case 2B is comparable with that at Case 1B during first 40 days of depressurization. Later the production rate steadily increases for Case 1B and reaches a peak of $\sim 2.75 \times 10^5 \text{ m}^3/\text{day}$ ($\sim 9.7 \text{ MMscf}/\text{day}$) after 5 months, while it stays at the relatively same level of $\sim 10^5 \text{ m}^3/\text{day}$ ($\sim 3.5 \text{ MMscf}/\text{day}$) for Cases 2B. A comparative analysis reveals that the production rate peak for Case 1B is associated with intensive decomposition of hydrate in sub-unit #18 facilitated by the water withdrawal from the underlying aquifer. After about 7 months the rate at Case 2B becomes larger than that at Case 1B resulting in 8×10^7 vs $6.5 \times 10^7 \text{ ST m}^3$ of gas volume produced, respectively, after 5 years. Because the water-bearing sand underlying sub-unit #18 has limited hydraulic communication with the producing well, water production is less for Case 2B than it is for Case 1B. For Case 1B the volumetric water/gas ratio drops within first several days of depressurization to a value close to 0.005 indicating that sensible heat supply to maintain the decomposition reaction becomes a leading factor influencing productivity.

2D property distribution

Figures 6-9 demonstrate 2D property distributions within first 20 (left figures) and 500 (right figures) meters from the well bore in Unit 4 for Case 1A at the 90-day time point. The pressure distributions show that the depressurization affect is limited to sub-unit #18 and the underlying aquifer. The pronounced depressurization of sub-unit #18 is interpreted because the highly-permeable (1000 md) water-bearing media located underneath the sub-unit. The temperature distributions reveal that temperature decreases in the areas where hydrate is decomposing and heat is consumed according to the endothermic nature of the dissociation reaction. That is consistent with hydrate and gas saturation distributions showing substantial hydrate decomposition in sub-unit #18 and limited propagation of the dissociation interfaces for the other sub-units. The distributions show that hydrate decomposes non-uniformly depending on thickness of hydrate-bearing and mud sub-units. The sub-units #1-17 develop well-defined vertical dissociation interfaces except for sub-unit #18, which forms both vertical and horizontal dissociation interfaces due to the presence of the aquifer.

Figures 10-13 capture 2D property distributions within first 20 (left figures) and 500 (right figures) meters from the well bore in Unit 4 for Case 1B at the 90-day time point. Pressure distributions demonstrate deep propagation of depressurization into Unit 4, such that for certain sub-units sandwiched between mud sections, the pressure reduction reaches 300-350 m from the well bore. The hydrate decomposition causes temperature drop and that is reflected in the temperature distribution figures. For about half of the reservoir volume the temperature declined from initial 18-20 to 15-18 °C. The hydrate saturation distributions display an interesting feature; - the hydrate decomposes at the horizontal interfaces developed at the boundaries between sand and mud sub-units. As temperature drops due to the decomposition reaction a temperature gradient between the sand and mud sections induces heat flux that support evolution of the horizontal interfaces. High initial effective permeability plays a decisive role in initiation and propagation of the interfaces throughout the reservoir in the lateral direction; opposite to Case 1A where low effective permeability precludes formation of horizontal interfaces. The dissociation at vertical interfaces is hindered by hydrate reformation behind them, such that hydrate saturation is raised above the initial 80% that reduces the amount of free water and effective permeability below the initial value. As a consequence, in the lateral direction hydrate is decomposed only within 1 m after 90 days of production. The interbedded architecture of the reservoir dictates flow of the mobile phases, released during decomposition, predominantly in the horizontal direction. As gas-saturated brine driven by a local pressure gradient approaches a dissociation interface, local pressure and temperature conditions may bring that gas out of solution and support the formation of secondary hydrate. That process is manifested as higher than initial hydrate saturations at the dissociation interfaces shown in the figures. For Cases "A", hydrate reformation behind the dissociation interface significantly hinders the productivity, in B Cases the horizontal dissociation interfaces provide an alternative path for gas to be delivered to the producing well and alleviate the adverse effect of reformation at the vertical interfaces. The hydrate reformation behind dissociation interfaces may be an artefact of 2D modeling and homogeneous descriptions of porosity, saturations, and intrinsic permeability assumed in this work for the formation units (Table 2).[21,35]

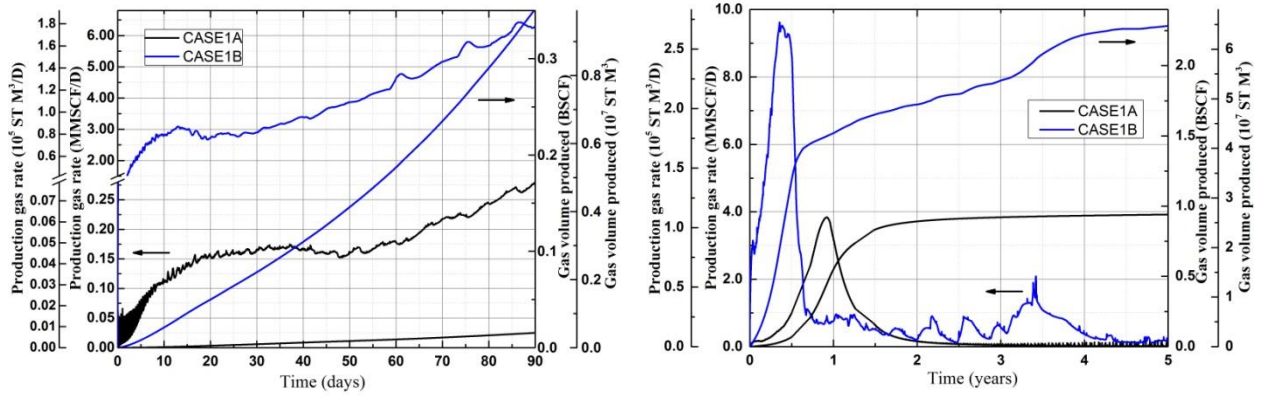


Figure 3: Cumulative production gas volumes and gas rates for 90 days (left) and 5 years (right) for the simulation Cases 1A and 1B.

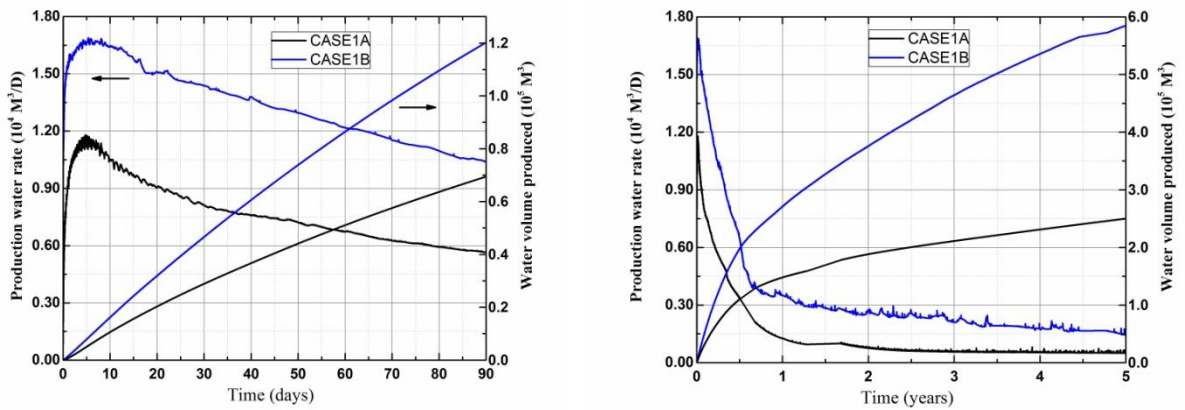


Figure 4: Cumulative production water volumes and water rates for 90 days (left) and 5 years (right) for the simulation Cases 1A and 1B.

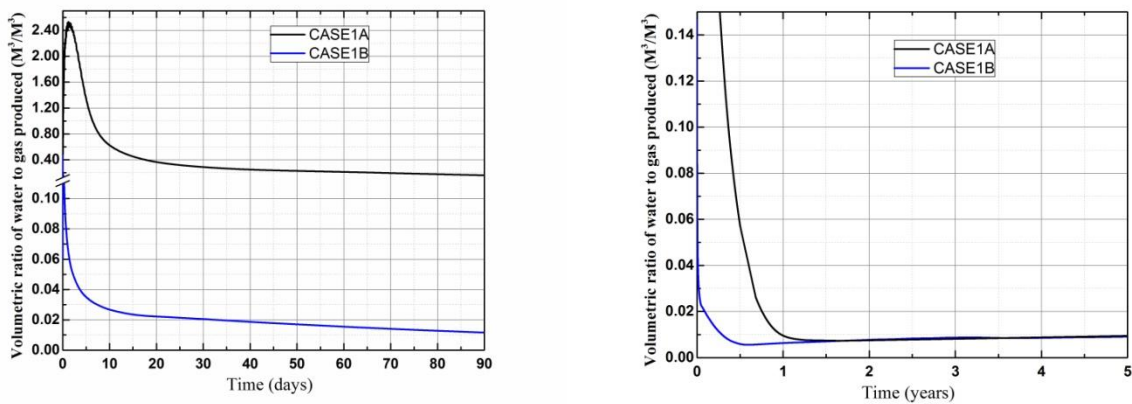


Figure 5: Cumulative production water volumes and water rates for 90 days (left) and 5 years (right) for the simulation Cases 1A and 1B.

**TIME 90 DAYS
CASE 1A**

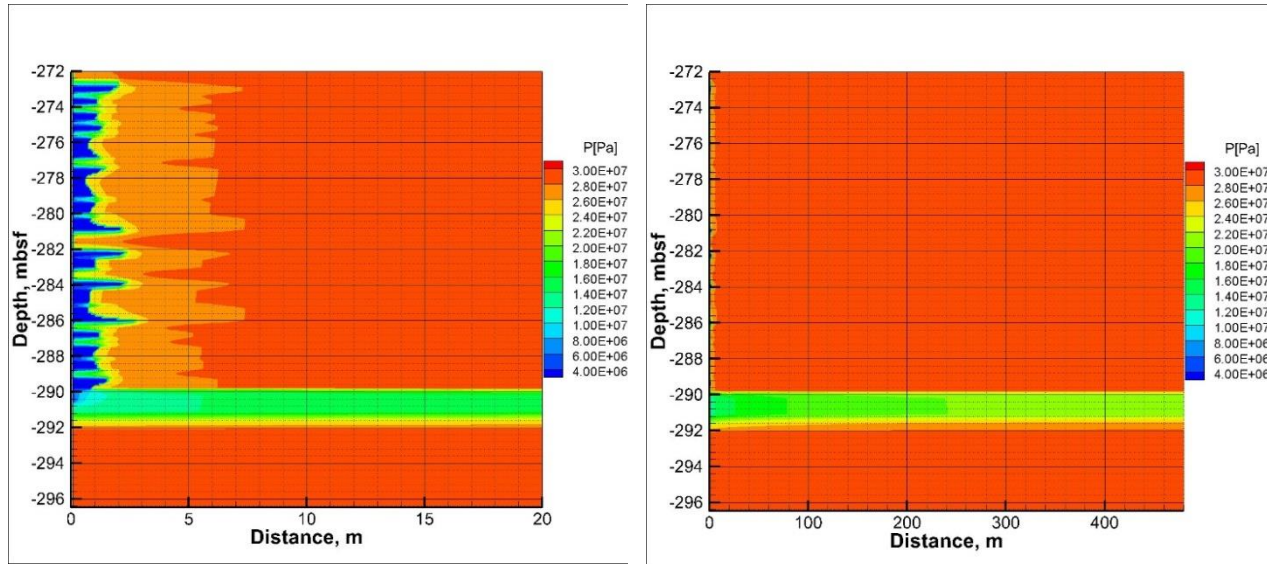


Figure 6: Pressure distribution within first 20 (left) and 500 (right) m from the well in UNIT 4.

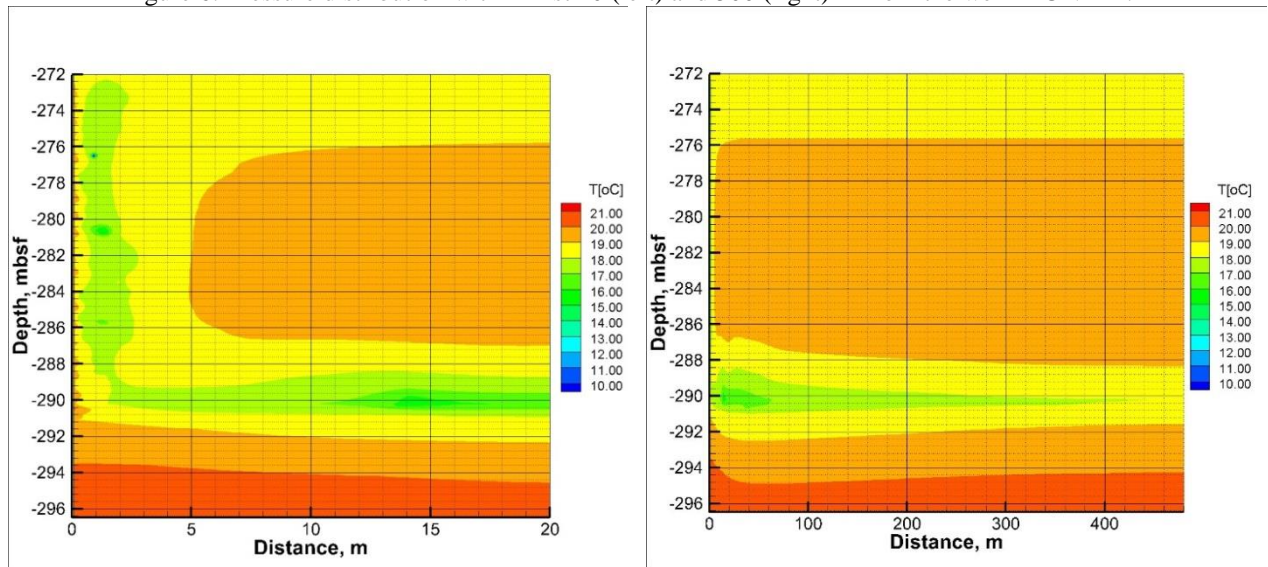


Figure 7: Temperature distribution within first 20 (left) and 500 (right) m from the well in UNIT 4.

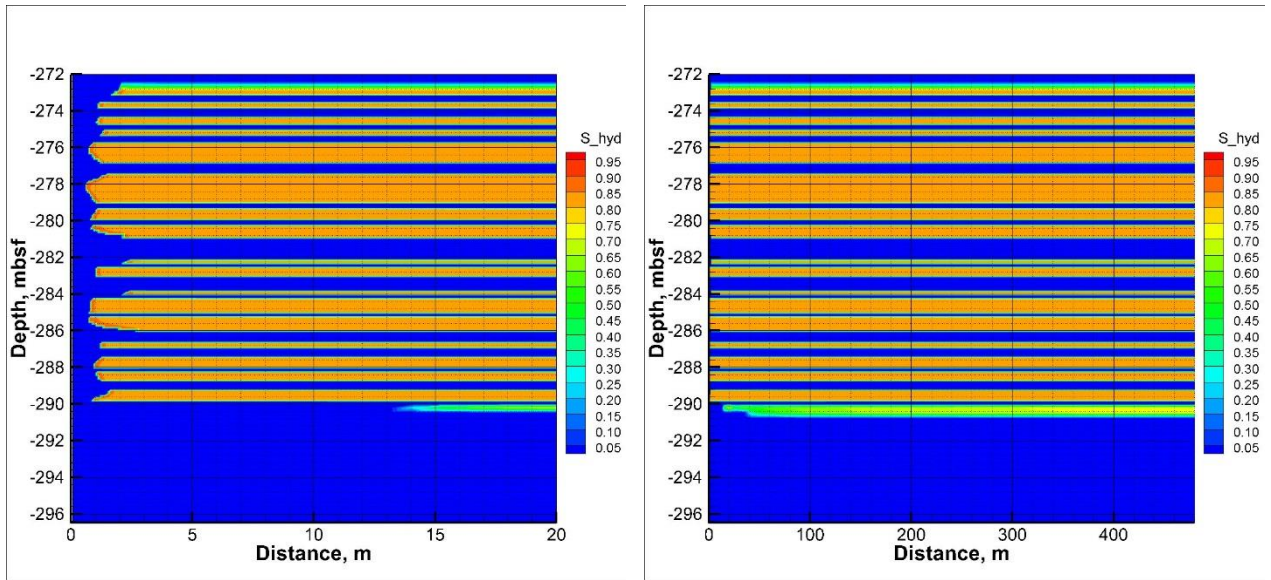


Figure 8: Hydrate saturation distribution within first 20 (left) and 500 (right) m from the well in UNIT 4.

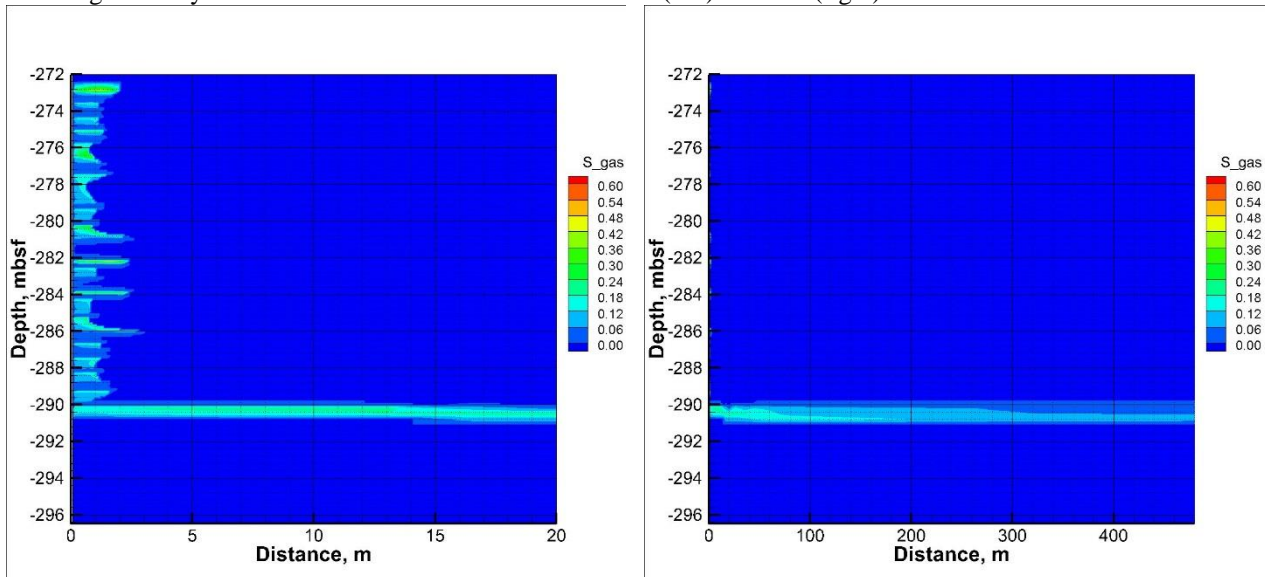


Figure 9: Gas saturation distribution within first 20 (left) and 500 (right) m from the well in UNIT 4.

**TIME 90 DAYS
CASE 1B**

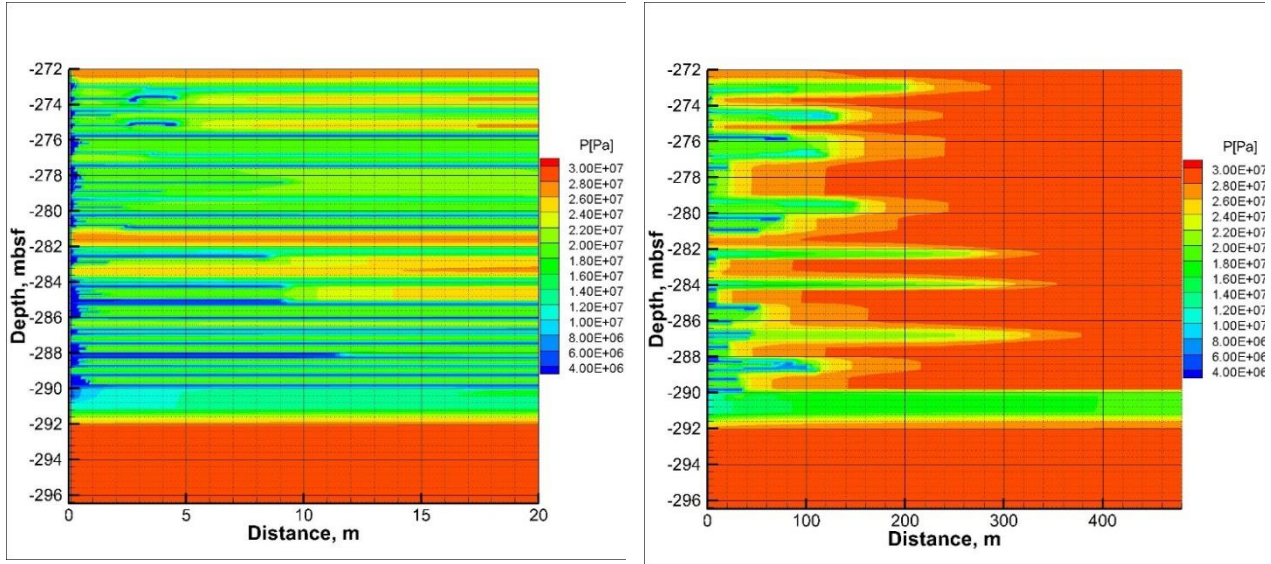


Figure 10: Pressure distribution within first 20 (left) and 500 (right) m from the well in UNIT 4

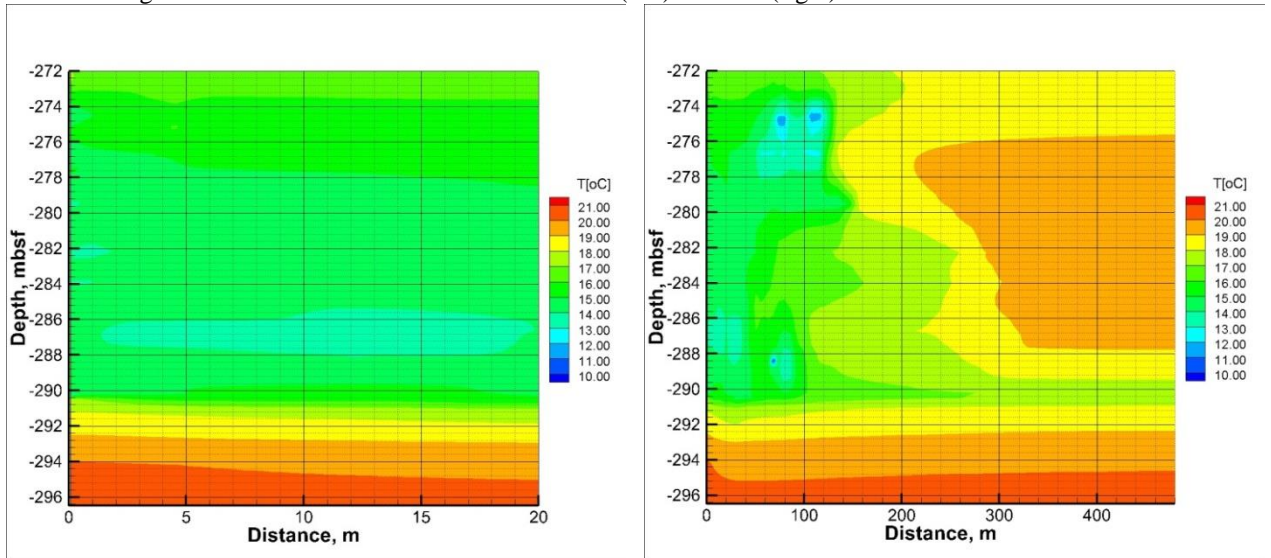


Figure 11: Temperature distribution within first 20 (left) and 500 (right) m from the well in UNIT 4

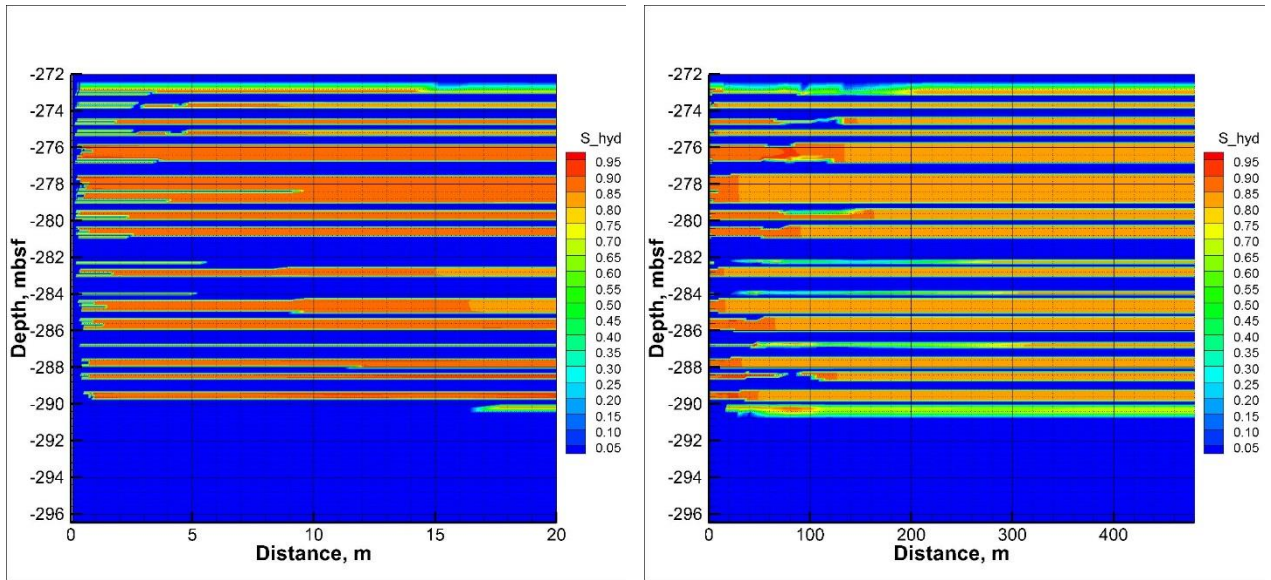


Figure 12: Hydrate saturation distribution within first 20 (left) and 500 (right) m from the well in UNIT 4.

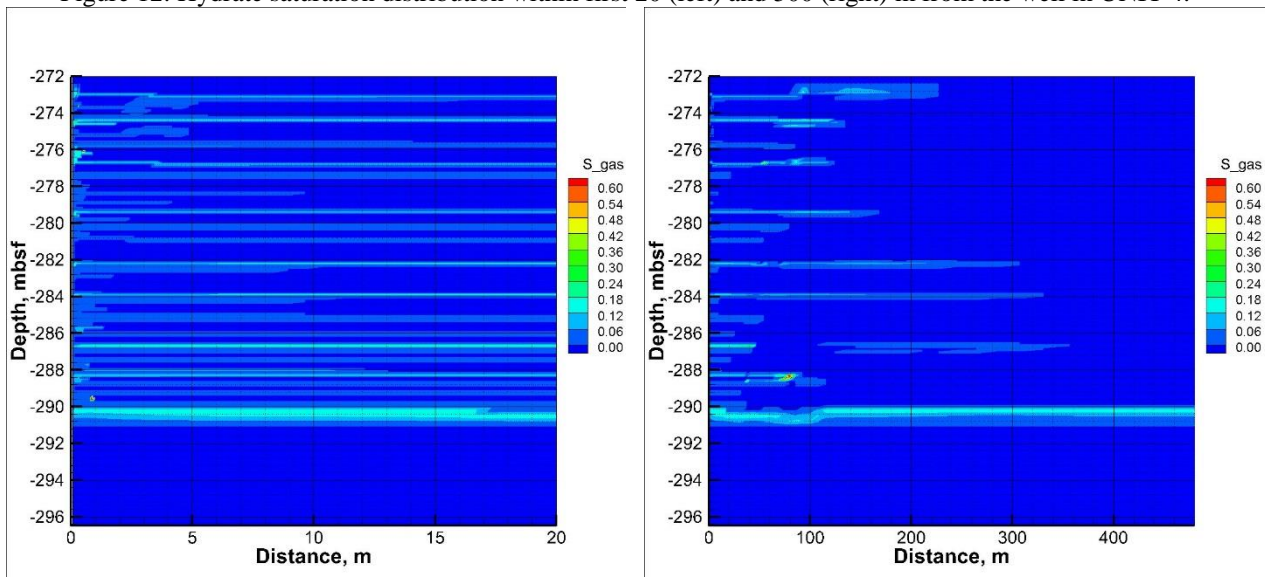


Figure 13: Gas saturation distribution within first 20 (left) and 500 (right) m from the well in UNIT 4.

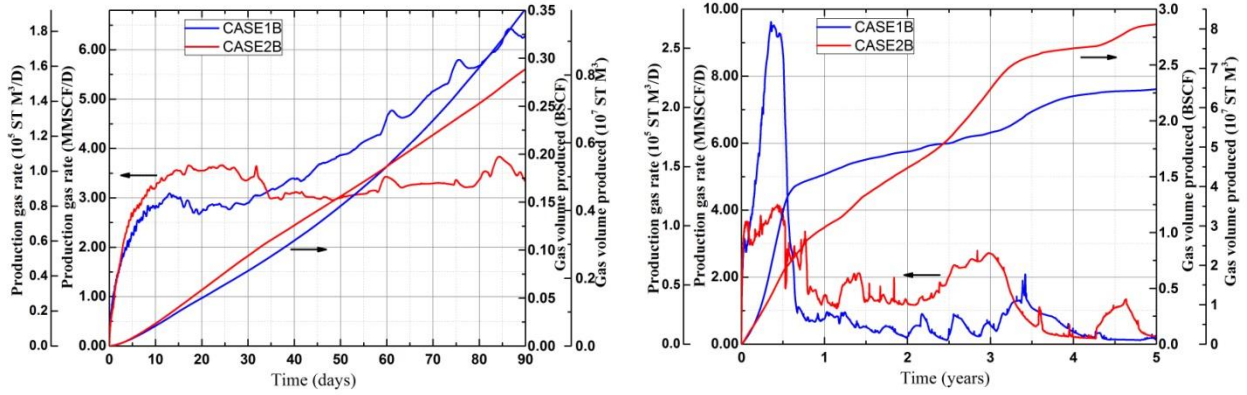


Figure 14: Cumulative production gas volumes and gas rates for 90 days (left) and 5 years (right) for the simulation Cases 1B and 2B.

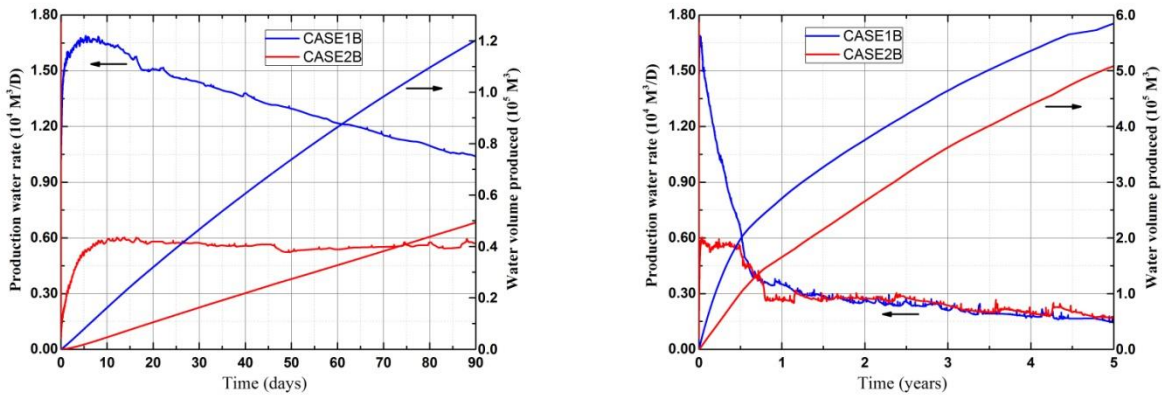


Figure 15: Cumulative production water volumes and water rates for 90 days (left) and 5 years (right) for the simulation Cases 1B and 2B.

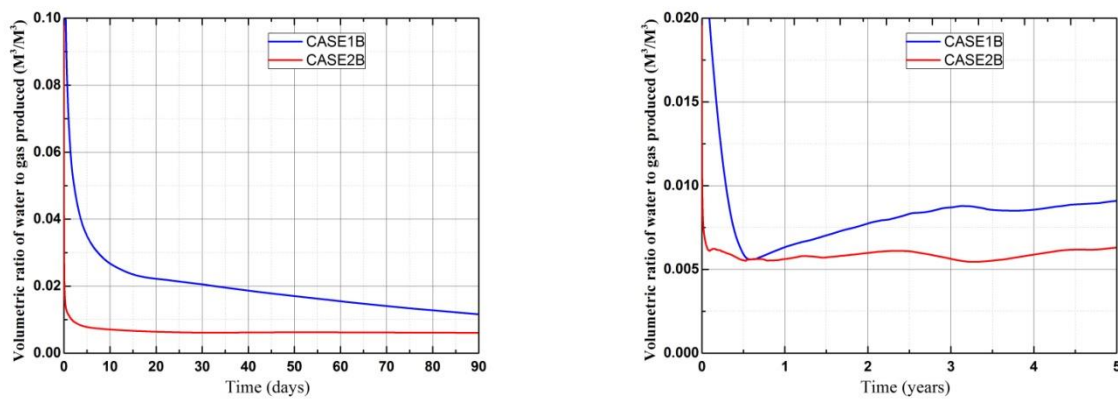


Figure 16: Cumulative production water volumes and water rates for 90 days (left) and 5 years (right) for the simulation Cases 1A and 1B.

Table 4: Daily average rates of gas and water produced, along with cumulative volumes.

Days	30	60	90
Case 1A			
Gas (m ³ /d)	4,636	5,010	7,863
Gas (cum.)	100,339	240,532	432,746
Water (m ³ /d)	811	673	564
Water (cum.)	28,887	51,066	69,447
Case 1B			
Gas (m ³ /d)	81,657	130,538	177,130
Gas (cum.)	2,205,050	5,271,170	9,899,780
Water (m ³ /d)	1,399	1,175	995
Water (cum.)	46,129	84,668	116,878
Case 2B			
Gas (m ³ /d)	94,835	96,534	93,777
Gas (cum.)	2,645,960	5,270,680	8,131,090
Water (m ³ /d)	573	538	570
Water (cum.)	16,247	32,715	49,341

Summary

The results of numerical simulations indicate that interbedded marine turbidite hydrate reservoirs are promising targets for gas production. Two production cases were created to explore reservoir response at low (Case 1A) and high (Cases 1B) initial (aqueous) effective permeabilities for the hydrate-bearing sand sub-units. The reservoir was predicted to produce gas at a rate from 7.86×10^3 m³/day (0.28 MMscf/day) to 1.77×10^5 m³/day (6.25 MMscf/day) after 90 days of depressurization for Case 1A and Case 1B, respectively. The broad range of the rates suggests that initial effective permeability plays crucial role in determining reservoir performance. Thus, it is important to engage core and well log permeability measurements to define lower and upper boundary values of effective permeabilities for simulations

The well completion design that limits production to sub-units #1 through #17 delivers similar production performance during first month of depressurization and provides larger produced gas volume after ~2.5 years in comparison with the well completed through sub-unit #18.

The analysis of pressure, temperature, hydrate, and gas saturation distributions show that hydrate dissociation occurs in a different fashion depending on an initial effective permeability value. For the low value (Cases “A”) the hydrate dissociates at well-defined vertically oriented interfaces receding from the well bore only by several meters over a 90-day time period. For the high value (Cases “B”) the presence of the interbedded mud sub-units, providing heat flux into the producing hydrate-bearing sand sub-units, results in developing of the horizontal dissociating interfaces along the boundaries between mud and sand layers of the reservoir. That process greatly enhances gas production potential and causes the hydrate decomposition to proceed by reduction of the hydrate body thickness within the sub-units, rather than by decreasing the lengths in the lateral direction.

The phenomenon of hydrate reformation attributed to homogenous approximation of the physical and hydrological parameters is exacerbated by the interbedded nature of the reservoir. Engaging heterogeneity to describe porosity/saturation/permeability in hydrate-bearing sub-units could ease the effect of reformation and allow a more

reliable evaluation of reservoir potential. Further refining is related to development of a 3D reservoir model that would utilize the expected fault-block geometry and allow a more precise estimation of long-term reservoir productivity.

Acknowledgment

The authors are thankful to Dr. William Waite of U.S. Geological Survey for providing estimations of thermal conductivities used in this paper. This technical effort was performed in support of the National Energy Technology Laboratory's ongoing research under the RES contract DE-FE0004000. Any use of trade, firm, or product names is for descriptive purposes only and does not imply endorsement by the U.S. Government.

Disclaimer

This project was funded by the Department of Energy, National Energy Technology Laboratory, an agency of the United States Government, through a support contract with AECOM. Neither the United States Government nor any agency thereof, nor any of their employees, nor AECOM, nor any of their employees, makes any warranty, expressed or implied, or assumes any legal liability or responsibility for the accuracy, completeness, or usefulness of any information, apparatus, product, or process disclosed, or represents that its use would not infringe privately owned rights. Reference herein to any specific commercial product, process, or service by trade name, trademark, manufacturer, or otherwise, does not necessarily constitute or imply its endorsement, recommendation, or favoring by the United States Government or any agency thereof. The views and opinions of authors expressed herein do not necessarily state or reflect those of the United States Government or any agency thereof.

References

- [1] E. D. Sloan, C. A. Koh, "Clathrate Hydrates of Natural Gas", 3rd ed.; Published by CRC Press: Boca Raton, FL., 2008.
- [2] K.A. Kvenvolden, "A primer on the geological occurrence of gas hydrate" Geological Society, London, Special Publications, 137, 9–30, 1998.
- [3] R. Boswell, and T. S. Collett, "Current perspectives on gas hydrate resources", *Energy and Environmental Science*, 4, 1206-1215, 2011.
- [4] R. Boswell, K. Yamamoto, S.-R. Lee, T. S. Collett, P. Kumar, S. Dallimore, S. Methane Hydrates. In: Letcher, T., ed., "Future Energy", 2nd Edition, Elsevier, 159-178, 2014.
- [5] T. Collett, A. Johnson, C. Knapp, R. Boswell, *AAPG Memoir*, 89, 2009.
- [6] M. Riedel, T.S. Collett, M.J. Malone, and the Expedition 311 Scientists, *Proc. Integrated Ocean Drilling Program*, IODP 311, Washington, D.C., doi:10.2204/iodp.proc.311.2006
- [7] Y. Tsujii, T. Fujii, M. Hayashi, R. Kitamura, M. Nakamizu, K. Ohbi, T. Saeki, K. Yamamoto, T. Namikawa, T. Inamori, N. Oikawa, S. Shimizu, M. Kawasaki, S. Nagakubo, J. Matsushima, K. Ochiai, T. Okui, *AAPG Memoir*, 89, 2009.
- [8] T. S. Collett, and R. Boswell, eds., "Resource and hazard implications of gas hydrates in the Northern Gulf of Mexico: Results of the 2009 Joint Industry Project Leg II Drilling Expedition", *J. Marine and Petroleum Geology*, 34, 1-224, 2012.
- [9] P. Kumar, T.S. Collett, K. Vishwanath, K.M. Shukla, J. Nagalingam, M.V. Lall, Y. Yamada, P. Schultheiss, M. Holland, "Gas Hydrate-Bearing Sand Reservoir Systems in the Offshore of India: Results of the India National Gas Hydrate Program Expedition 02", *Fire in the Ice*, 16, 1-8, 2016.
- [10] N. Wu, H. Zhang, X. Su, "High concentrations of hydrate in disseminated forms found in very fine-grained sediments of Shenhu area, South China Sea", *Terra Nostra*, 1-2, 236–237, 2007.

- [11] C. Hadley, D. Peters, A. Vaughn, D. Bean, D., “Gumusut-Kakap project: geohazard characterization and impact on field development plans”, *Proceedings, IPTC Conference*, IPTC -12554, 2008.
- [12] K. P. Park, “Gas hydrate exploration activities in Korea”, *Proceedings, 6th International Conference on Gas Hydrates*, 2008.
- [13] M.V. Ramana, T. Ramprasad, T. S. Collett, P. Kumar, R. M. Boswell, M. Riedel, A.V. Sathe, M. Lall, K. Vishwanath, A. Muzumdar, K. Sain, J. Cochran, eds., “Geologic implications of gas hydrates in the offshore of India: Results of the National Gas Hydrate Program Expedition 01”, *J. Marine and Petroleum Geology*, 58, Part A, 1-550, 2014.
- [14] Y. Konno, T. Fujii, A. Sato, K. Akamine, M. Naiki, Y. Masuda, K. Yamamoto, J. Nagao, “Key Findings of the World’s First Offshore Methane Hydrate Production Test off the Coast of Japan: Toward Future Commercial Production”, *Energy and Fuels*, 2017.
- [15] M. Gaddipati, B. J. Anderson, “3D Reservoir modeling of depressurization-induced gas production from gas hydrate reservoirs at the Walker Ridge site, Northern Gulf of Mexico”, *Offshore Technology Conference*, OTC-23582-MS, 2012.
- [16] E. M. Myshakin, M. Gaddipati, K. Rose, K., B. J. Anderson, “Numerical simulations of depressurization-induced gas production from gas hydrate reservoirs at the Walker Ridge 313 site, northern Gulf of Mexico”, *J. Marine and Petroleum Geology*, 34, 169–185, 2012.
- [17] G. J. Moridis, J. Kim, M. T. Reagan, S.-J. Kim, “Feasibility of gas production from a gas hydrate accumulation at the UBGH2-6 site of the Ulleung basin in the Korean East Sea”, *Journal of Petroleum Science and Engineering*, 108, 180-210, 2013.
- [18] S. Zheng, G.J. Moridis, K. Zhang, R. Yang, N. Wu, “Numerical investigation of gas production strategy for the hydrate deposits in the Shenhu area”, *Offshore Technology Conference*, OTC-20551, 2010.
- [19] M. Kurihara, A. Sato, H. Ouchi, H. Narita, T. Ebinuma, K. Suzuki, Y. Masuda, “Prediction of production test performances in Eastern Nankai Trough methane hydrate reservoirs using 3D reservoir model”, *Offshore Technology Conference*, OTC-20737, 2010.
- [20] M. Zhou, K. Soga, E. Xu, S. Uchida, K. Yamamoto, “Numerical study on Eastern Nankai Trough gas hydrate production test”, *Offshore Technology Conference*, OTC-25169-MS, 2014.
- [21] R. Boswell, T. Collett, E. Myshakin, T. Ajayi, Y. Seol, “The Increasingly Complex Challenge of Gas Hydrate Reservoir Simulation”, *Proceedings, 9th International Conference on Gas Hydrates*, 2017.
- [22] S. Dai, R. Boswell, W. F. Waite, J. Jang, J.-Y. Lee, Y. Seol, “What has been Learned from Pressure Cores”. *Proceedings, 9th International Conference on Gas Hydrates*, 2017.
- [23] J. F. Wright, S. R. Dalimore, F. M. Nixon, “Influence of grain size and salinity on pressure-temperature thresholds for methane hydrate stability in JAPEX/JNOC/GSC Mallik 2L-38 gas hydrate research-well sediments. In Scientific Results from JAPEX/JNOC/GSC Mallik 2L-38 Gas Hydrate Research-Well Mackenzie, Delta, Northwest Territories, Canada”, *Geological Survey of Canada*, Bulletin 544, 1999.
- [24] G. R. Dickens, M. S. Quinby-Hunt, “Methane hydrate stability in pore water: a simple theoretical approach for geophysical applications,” *J. Geophys. Res.*, 102, 773–783, 1997.
- [25] G. J. Moridis, M. B. Kowalsky, K. Pruess, “Depressurization induced gas production from Class 1 hydrate deposits”, *Annual Technical Conference and Exhibition*, SPE-97266, 2005.
- [26] G. T. Moridis, M. T. Reagan, “Gas production from oceanic Class 2 hydrate accumulations”, *Offshore*

Technology Conference, OTC-18866, 2007.

- [27] J. C. Santamarina, S. Dai, M. Terzariol, J. Jang, W.F. Waite, W.J. Winters, J. Nagao, J. Yoneda, Y. Konno, T. Fujii, K. Suzuki, “Hydro-bio-geomechanical properties of hydrate-bearing sediments from Nankai Trough”, *J. Marine and Petroleum Geology*, 66, 434-450, 2015.
- [28] B.J. Anderson, M. Kurihara, M. D. White, G. J. Moridis, S. J. Wilson, M. Pooladi-Darvish, M. Gaddipati, Y. Masuda, T. S. Collett, R. B. Hunter, H. Narita, K. Rose, R. Boswell, R., “Regional long-term production modeling from a single well test, Mount Elbert gas hydrate stratigraphic test well, Alaska North Slope”, *J. Marine and Petroleum Geology*, 28, 493-501, 2011.
- [29] Y. Konno, J. Yoneda, K. Egawa, T. Ito, Y. Jin, M. Kida, K. Suzuki, T. Fujii, J. Nagao, “Permeability of sediment cores from methane hydrate deposit in the Eastern Nankai Trough”, *J. Marine and Petroleum Geology*, 66, 487-495, 2015.
- [30] G. J. Moridis, “User’s Manual for the HYDRATE v1.5 Option of TOUGH+ v1.5: A Code For The Simulation Of System Behavior In Hydrate-Bearing Geologic Media”, Report LBNL-6869E, Lawrence Berkeley National Laboratory, 2014.
- [31] J. C. Maxwell, “A Treatise on Electricity & Magnetism”, Dover Publications Inc., 1954.
- [32] M. T. Van Genuchten, *Soil Sci. Society*, 44, 892-900, 1980.
- [33] R. H. Brooks, A. T. Corey, “Hydraulic properties of porous media”, *Hydrology Papers*, 3, 1964.
- [34] B. Anderson, S. Hancock, S. Wilson, C. Enger, T. Collett, R. Boswell, R. Hunter, “Formation pressure testing at the Mount Elbert Gas Hydrate Stratigraphic Test Well, Alaska North Slope: Operational summary, history matching, and interpretations”, *J. Marine and Petroleum Geology*, 28, 478-492, 2011.
- [35] E. Myshakin, T. Ajayi, B. Anderson, Y. Seol, R. Boswell, “Numerical Simulations of Depressurization-induced Gas Production from Gas Hydrates Using 3-D Heterogeneous Models of L-Pad, Prudhoe Bay Unit, North Slope Alaska”, *J. Natural Gas Science and Engineering*, 35, 1336-1352, 2016.